Evaluation of Shaft Angle Effects on Dynamic Stall Based on Low- and High-Fidelity Aero-Elastic Rotor Simulations

Ilyès Berhouni
Research scientist
DAAA, ONERA
Institut Polytechnique de Paris
92190 Meudon, France

Joëlle Bailly
Research scientist
DAAA, ONERA
Institut Polytechnique de Paris
92190 Meudon, France

François Richez
Research scientist
DAAA, ONERA
Institut Polytechnique de Paris
92190 Meudon, France

ABSTRACT

This paper investigates the effect of tilting a rotor backward on dynamic stall at a moderate advance ratio using low-fidelity (free wake) and high-fidelity (Computational Fluid Dynamics) approaches. The first objective pursued is to evaluate the capability of the low-fidelity approach to provide accurate results for such flight conditions. A second objective is to precisely identify the evolution of the mechanisms leading to dynamic stall under high-load conditions. The low-fidelity approach is found to predict the main features of the blade-vortex interaction leading to dynamic stall on the retreating blade, with a lower intensity compared to high-fidelity results (especially when the rotor is tilted backward). It however misses a second dynamic stall event occurring on the rear blade that is mainly due to an interaction with root and stall vortices. This leads to slightly different values and trends of thrust coefficients with respect to the collective pitch angle near stall compared to high-fidelity results.

NOTATION

A	Rotor disk area, πR^2, $[m^2]$
a_∞	Speed of sound, $[m.s^{-1}]$
c	Rotor blade chord length, $[m]$
C_mM^2	Section pitching moment coefficient, $\frac{M_y}{0.5\rho_\infty a_\infty^2 c^2}$, [-]
C_nM^2	Section normal force coefficient, $\frac{f_n}{0.5\rho_\infty a_\infty^2 c}$, [-]
C_T	Rotor thrust coefficient, $\frac{T}{\rho_\infty A(\omega R)^2}$, [-]
C_Q	Rotor power coefficient, [-]
f_n	Section aerodynamic normal force, $[N.m^{-1}]$
M	Mach number, [-]
M_y	Section pitching moment, $[N]$
N_b	Number of rotor blades, [-]
Q	Q-criterion, $[s^{-2}]$
R	Rotor radius, $[m]$
r	Radial location, $[m]$
T	Rotor thrust, $[N]$
V_h	Rotorcraft velocity, $[m.s^{-1}]$
α_s	Shaft angle, $[deg]$
θ_0	Collective pitch angle, $[deg]$
θ_{1c}	Lateral cyclic pitch angle, $[deg]$
θ_{1s}	Longitudinal cyclic pitch angle, $[deg]$
μ	Rotor advance ratio, $\frac{V_h}{\omega R}$, [-]
ρ_∞	Freestream density, $[kg.m^{-3}]$
σ	Rotor solidity, $\frac{N_b c}{\pi R}$ [-]
ω	Rotor angular velocity, $[rad.s^{-1}]$
ψ	Azimuth angle, $[deg]$

INTRODUCTION

New architectures of aircraft dedicated to high-speed flight combine a main rotor with propellers which respectively provide lift and thrust. In the last decades, several architectures of this type have been developed (such as the Sirkorsky S-97 RAIDER (Ref. 10) and the Airbus Helicopters RACER (Ref. 6)), with a particular focus on military purposes. These types of aircraft are designed to reach higher velocities than classical architectures while remaining able to perform maneuvers that involve tilting the rotor backwards, which can lead to dynamic stall.

Several numerical approaches can be considered in order to investigate dynamic stall. Among them, a coupling between a comprehensive analysis (CA) structural code and another tool for the analysis or the modelling of the fluid dynamics is widely found in the literature. The associated degree of

Funded by the European Union

Funded by the European Union. Views and opinions expressed are however those of the authors only and do not necessarily reflect those of the European Union. Neither the European Union nor the granting authority can be held responsible for them.

accuracy varies with the complexity of the numerical methods and the physical modelling considered.

Multiple low-fidelity approaches consist in a coupling between a CA structural code and an induced velocity model. They are commonly considered as not adapted to predict dynamic stall conditions. This conclusion is however generally drawn with induced velocity models that are too simple to be able to capture blade-vortex interaction (BVI) phenomena. Considering more complex induced velocity models based on a free wake modelling could be more adapted to such investigations, yet a lack of literature tackling this problematic is observed. Additional studies investigating the capability of low-fidelity approaches involving a free wake modelling to predict dynamic stall are thus required, especially when this phenomenon is triggered by BVI.

Regarding high-fidelity approaches, a coupling between a CA structural code and a computational fluid dynamics (CFD) solver can be considered. The accuracy of this type of coupling has been thoroughly validated in the past for the analysis of dynamic stall in negative (i.e. forward-tilted rotor) or close to zero shaft angle conditions. This validation was performed for full-scale rotors (such as the UH-60A (Refs. 13, 14)), as well as for model scaled rotors (such as 7A (Refs. 12, 19) and ERATO (Refs. 1, 18)). The origin of physical phenomena leading to dynamic stall was analysed in (Refs. 5, 15, 17), showing the major role of BVI. On the other hand, limited literature can be found on the physical mechanisms leading to dynamic stall in turn flight (i.e. backward-tilted rotor) (Ref. 9). It focuses on the analysis of dynamic stall for a moderate-speed turn flight using a high-fidelity CA/CFD coupling, and highlights the complex and unsteady flow nature involving shock-induced separation, BVI and trailing edge separation.

Therefore, this paper presents numerical simulations performed at the onset of dynamic stall on a generic rotor at both null and high positive shaft angles using low- and high-fidelity simulation tools. A first objective is to investigate the capability of low-fidelity approaches (CA coupled with free wake induced velocity model) to accurately investigate dynamic stall for these flight conditions, using the high-fidelity results as a reference. A second objective is to provide a detailed analysis of the effect of a high positive value of the rotor shaft angle on the stall limit of the rotor at moderate speed.

In a first section, the low- and high-fidelity methods used to perform the numerical simulations will be presented, as well as their respective numerical setups. The mechanisms leading to dynamic stall will then be analysed using both the low- and high-fidelity results. Potential differences between the two approaches will also be investigated, and the validity of the low-fidelity coupling to analyse dynamic stall at these flight conditions will be assessed. In a final section, the high-fidelity results will be further analysed in order to investigate in detail the effect of the shaft angle increase on the mechanisms leading to dynamic stall. Conclusions on the results obtained and perspectives for future works will be presented at the end of this paper.

While this paper focuses on the effect of strong loads on dynamic stall, another aspect that can strongly influence the stall mechanisms is the helicopter velocity. The effect of increasing the helicopter speed from moderate to high values is investigated in detail in a second paper proposed by the authors (Ref. 16), using the same generic rotor and numerical approaches. Both activities are part of the same task of the European Next Generation Rotorcraft Technologies (ENGRT) project funded by the European Union.

PRESENTATION OF THE TEST CASE AND OF THE NUMERICAL APPROACHES

Description of the test case

The test case selected for the study presented in this paper that is common to the two approaches is a five-bladed generic rotor with a constant twist and a parabolic tip. In the two approaches presented in the following, a fixed collective pitch angle θ_0 value was fixed as input and a trim law ensuring null values of cyclic flap angles (with the cyclic pitch angles θ_{1c} and θ_{1s} as free trim parameters) was imposed. A fixed advance ratio $\mu = 0.35$ corresponding to a moderate forward flight velocity with a nominal rotation velocity was selected, and two shaft angle values $\alpha_s = 0°$ (flat rotor) and $\alpha_s = 10°$ (backward-tilted rotor) were investigated.

Presentation of the low-fidelity approach: STORM/MINT

The low-fidelity analysis is based on the new version of the CA code HOST (Ref. 3) named STORM, supplemented by the time marching free wake model MINT (Ref. 8). The aerodynamic model is based on a lifting-line analysis, and a simplified beam model is used to describe the blade structure. The sensitivity of the results to the number of sections selected to discretize the blade, the time step used in the wake model, the flexibility of the blade and the wake computation (rigid or pure free wake) was investigated. Following the results obtained, 25 aerodynamic sections were selected for the blade discretization, the time step was fixed at 6°/iteration, a rigid wake model was selected and the blade was assumed flexible with its dynamic response computed using eight modes and eight harmonics. The simulations were performed during 30 revolutions in order to ensure that the wake and the rotor loads were stabilised. Five revolutions of the wake were preserved at the end of the simulation, on which a mean was performed to compute the different aerodynamic coefficients. In addition, while MINT is selected as the preferred wake model, different possibilities have been investigated in this study to provide a complete comparison:

- Meijer-Drees (M.-D.), based on a simple analytical formula of the induced velocity.
- Finite State Wake (FSW), which improves the prediction of M.-D. by considering a highly non-uniform inflow distribution (Ref. 2).

- METAR, based on a steady wake model composed of vortex segments with a prescribed geometry and that induces inflow velocity on the rotor disk.

The low computational cost of this method allowed to investigate a large number of collective pitch angle θ_0 values ranging between -4° and 8° with a step of 0.5°.

Presentation of the high-fidelity approach: HOST/elsA

The high-fidelity approach involves a computational fluid dynamics (CFD)/CA loose coupling between the ONERA-SAFRAN software elsA (Ref. 4) and HOST (Ref. 3). A classical Chimera overset grid technique with blade-fitted grids and a cartesian background grid was used (cf. Fig. 1). Each blade grid is composed of 3.2 million cells (208 points along the blade chord, 65 in the direction normal to the wall and 235 in the spanwise direction). The background mesh is composed of 39 million cells, with a cell size in the rotor area fixed to 10% of the blade reference chord. The Unsteady Reynolds-Averaged Navier Stokes (URANS) equations supplemented by the two-equations $k-\omega$ turbulence model proposed by Kok (Ref. 7) with Menter's SST correction (Ref. 11) were solved in the CFD simulations. The convective flux is discretized using a second-order Jameson centered scheme with artificial dissipation, with its dissipation coefficients fixed at $\chi_2 = 0.5$ and $\chi_4 = 0.008$. The time integration is based on a second-order implicit Gear method, using a 0.25°/iteration time step and 30 Newton sub-iterations.

Due to the higher cost of this approach, a lower number of flight conditions were selected using the low-fidelity results to estimate the conditions at which dynamic stall should occur. For the flat rotor ($\alpha_s = 0°$), collective pitch angle values of $-1°, 1°, 4°, 5°$ and $6°$ were simulated. For the backward-tilted position of the rotor ($\alpha_s = 10°$), collective pitch angle values of $-6°, -4°, -2°, 0°$ and $1°$ were considered. The coupling iterations were performed until the values of the cyclic pitch angles and of the rotor thrust coefficient C_T/σ were stabilised. These numerical simulations provided information to investigate the validity of the low-fidelity approach on these operating regimes, as well as data regarding the physical phenomena at the origin of dynamic stall.

COMPARISON BETWEEN LOW- AND HIGH-FIDELITY RESULTS

In this section, two objectives will be pursued. Firstly, the results obtained with HOST/elsA will be systematically compared to those obtained with STORM/MINT in order to evaluate the capability of the low-fidelity approach to provide consistent results for the flight conditions investigated. Secondly, the results obtained for $\alpha_s = 0°$ and $\alpha_s = 10°$ will be used to investigate the effect of tilting the rotor backward on dynamic stall. To better evaluate the sensitivity of the results to the induced velocity model in the low-fidelity approach, additional results obtained with M.-D., FSW and METAR will also be commented in the polars.

First of all, the polars of performance coefficients and control angles obtained with both low- and high-fidelity approaches are plotted for $\alpha_s = 0°$ and $\alpha_s = 10°$ in Fig. 2. Concerning the cyclic pitch angles, all the induced velocity models provide similar results at $\alpha_s = 0°$ and $\alpha_s = 10°$, except for M.-D. that tends to underestimate the lateral cyclic pitch θ_{1c} and to overestimate the longitudinal cyclic pitch θ_{1s}. The HOST/elsA simulations give values of θ_{1c} comprised between HOST/FSW and STORM/MINT, as well as θ_{1s} values that are similar to the other models. Note that HOST/METAR appears to be in very good agreement with HOST/elsA at $\alpha_s = 0°$, a result that might however be fortuitous as STORM/MINT is in better agreement with CFD at $\alpha_s = 10°$.

In terms of rotor thrust C_T/σ, Fig. 2 highlights a larger scattering of the results. The different models and approaches provide similar trends, with a linear increase of the thrust coefficient with respect to θ_0 until dynamic stall occurs. At $\alpha_s = 0°$, MINT provides the lowest thrust values and M.-D. the highest ones with a maximum difference of roughly 0.03 (i.e. 30%), while FSW and METAR predictions lie in between. The slope of the $C_T/\sigma(\theta_0)$ curve is also very different between the models. Consequently, while rotor thrust values are similar between the different models at low θ_0 values, discrepancies become more significant as the collective pitch angle increases. Finally, dynamic stall does not occur at the same values of $(C_T/\sigma, \theta_0)$ between the different models investigated. METAR and M.-D. are in good agreement on the prediction of collective pitch angles at which dynamic stall occurs, with thrust values remaining close to constant for $\theta_0 \geq 5.5°$, while FSW predicts stall to occur at $\theta_0 = 4°$. METAR and FSW are on the other hand in better agreement in terms of C_T/σ values attained at stall (roughly 0.12) compared to M.-D., as the latter predicts higher thrust values (roughly 0.13). MINT predicts a higher value of $\theta_0 = 8°$ above which dynamic stall occurs with a maximum thrust $C_T/\sigma_{stall} = 0.116$, while HOST/elsA predicts dynamic stall close to $\theta_0 = 6°$ with a maximum thrust of $C_T/\sigma = 0.12$. Increasing the shaft angle to $\alpha_s = 10°$ leads to higher thrust values attained along a large part of the polar for all the methods investigated. Similar observations and thrust values are however observed at stall for FSW, METAR and M.-D, with dynamic stall however occurring at lower values of θ_0 compared to the flat rotor results (which is consistent since the shaft angle is tilted backward). The STORM/MINT and HOST/elsA results on the other hand lead to different trends near stall compared to the flat rotor case. Both approaches predict that higher thrust coefficient values are obtained, and that the occurrence of dynamic stall is less instantaneous with a slope change that is more progressive out of the linear increase region. The results between these two approaches also appear in better agreement in the linear thrust increase region, with differences that become more visible at higher values of θ_0. Note that this last result is again representative of different slopes predicted by HOST/elsA and STORM/MINT: the first approach gives lower thrust values at low collective pitch angles and higher values than the second approach otherwise.

The analysis of the rotor power coefficient in Fig. 2 leads to

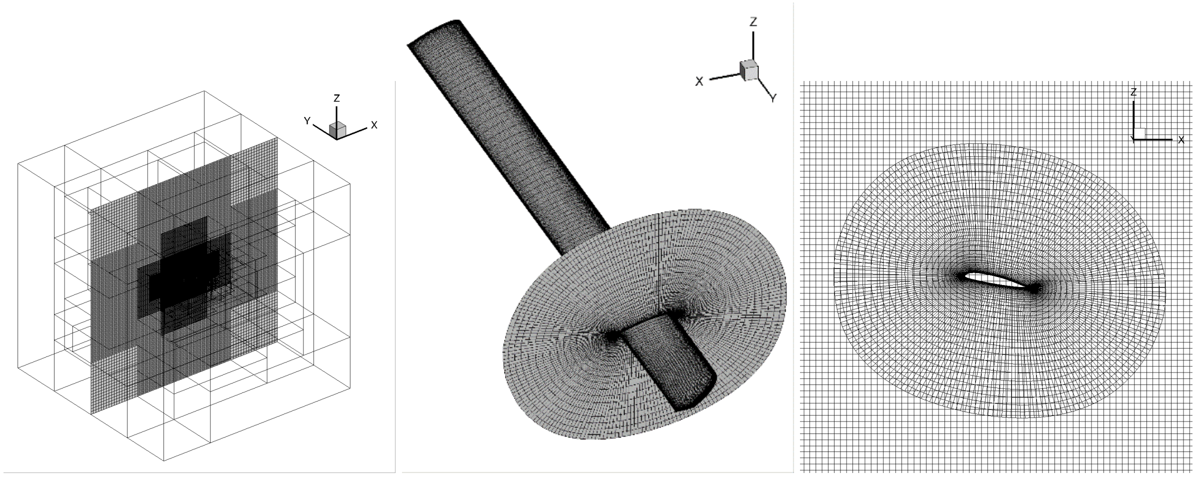

Figure 1: Background (left) and blade (middle) meshes with a visualisation of the overlapping region (right).

opposite observations with respect to the thrust coefficient. Similar values are obtained with all the different models investigated at $\alpha_s = 0°$, with on the other hand a larger scattering of the results at $\alpha_s = 10°$. M.-D. tends to underestimate the values of C_Q/σ while STORM/MINT tends to overestimate them. The HOST/elsA results lie in between those obtained with the different models investigated.

The evolution of the blade thrust with respect to the azimuth ψ obtained with HOST/elsA and STORM/MINT is then shown in Fig. 3 to analyse more in detail the rotor thrust. At $\alpha_s = 0°$, the trends obtained are very similar between the two approaches, with commonly-observed peaks of thrust generation located around $\psi = 0°$ and $\psi = 180°$. The main difference visible between the two approaches is that HOST/elsA predicts slightly higher peak values at these azimuth angles with respect to STORM/MINT, which explains the higher values of thrust coefficient obtained in Fig. 2.

Increasing the shaft angle to $\alpha_s = 10°$ leads to several effects on the blade thrust evolution. At low collective pitch angles ($\theta_0 \leq -2°$), the agreement between the low- and high-fidelity approaches is satisfactory. The amplitude and the phase of the evolution of the blade thrust are rather similar, with however a slightly higher harmonic content with HOST/elsA close to $\psi = 0°$. At higher collective pitch angles ($\theta_0 \geq 0°$), noticeable discrepancies appear due to stronger oscillations at high-harmonics with HOST/elsA simulations on the advancing blade side. This particular difference will be further investigated using the following results.

In order to understand the differences observed between STORM/MINT and HOST/elsA, blade section airloads will next be analysed together with the blade torsion deformation. For a given shaft angle value, the HOST/elsA and STORM/MINT results will be compared at an identical collective pitch angle value in order to investigate the differences between the two approaches. This will allow to investigate the differences in the results obtained with the low-and high-fidelity approaches when being given an identical trim law.

To analyse the effect of a shaft angle increase, specific flight conditions with similar rotor thrust coefficient values predicted by HOST/elsA are selected to be compared:

- Results obtained for (α_s, θ_0) = (0°,1°) will be compared to those obtained for (α_s, θ_0) = (10°,-4°) as they respectively give $(C_T/\sigma)_{HOST/elsA} = 0.0923$ and $(C_T/\sigma)_{HOST/elsA} = 0.0965$.
- Results obtained for (α_s, θ_0) = (0°,6°) will be compared to those obtained for (α_s, θ_0) = (10°,0°) as they respectively give $(C_T/\sigma)_{HOST/elsA} = 0.1213$ and $(C_T/\sigma)_{HOST/elsA} = 0.1220$.

The section normal force coefficients C_nM^2 obtained with HOST/elsA and STORM/MINT for the above cases are shown in the form of rotor maps in Figs. 4 and 5. Note that it would also be relevant to compare results obtained with the low-and high-fidelity approaches for an identical thrust coefficient value. The polars plotted in Fig. 2 however show that STORM/MINT does not predict sufficiently high thrust coefficient values as dynamic stall occurs to allow such a comparison.

First of all, let us consider the rotor maps corresponding to the moderately-loaded cases in Fig. 4. Despite the discrepancies observed in terms of rotor thrust coefficients, the contours obtained with STORM/MINT and HOST/elsA at both shaft angle values are very similar. In these cases the lift is mainly generated on the rear blade between $\psi = 330°$ and $\psi = 0°$, with differences mainly observed in the amplitude predicted by the low- and high-fidelity approaches. Additionally, a region of negative lift generation can be observed close to $\psi = 120°$ on all the rotor maps of Fig. 4 The increase of shaft angle moderately impacts the rotor maps obtained, with two main evolutions visible with both STORM/MINT and HOST/elsA in the first and second quadrants. HOST/elsA predicts a region of increased lift generation due to the backward-tilting of the rotor between $\psi = 90°$ and $\psi = 120°$, and a region of

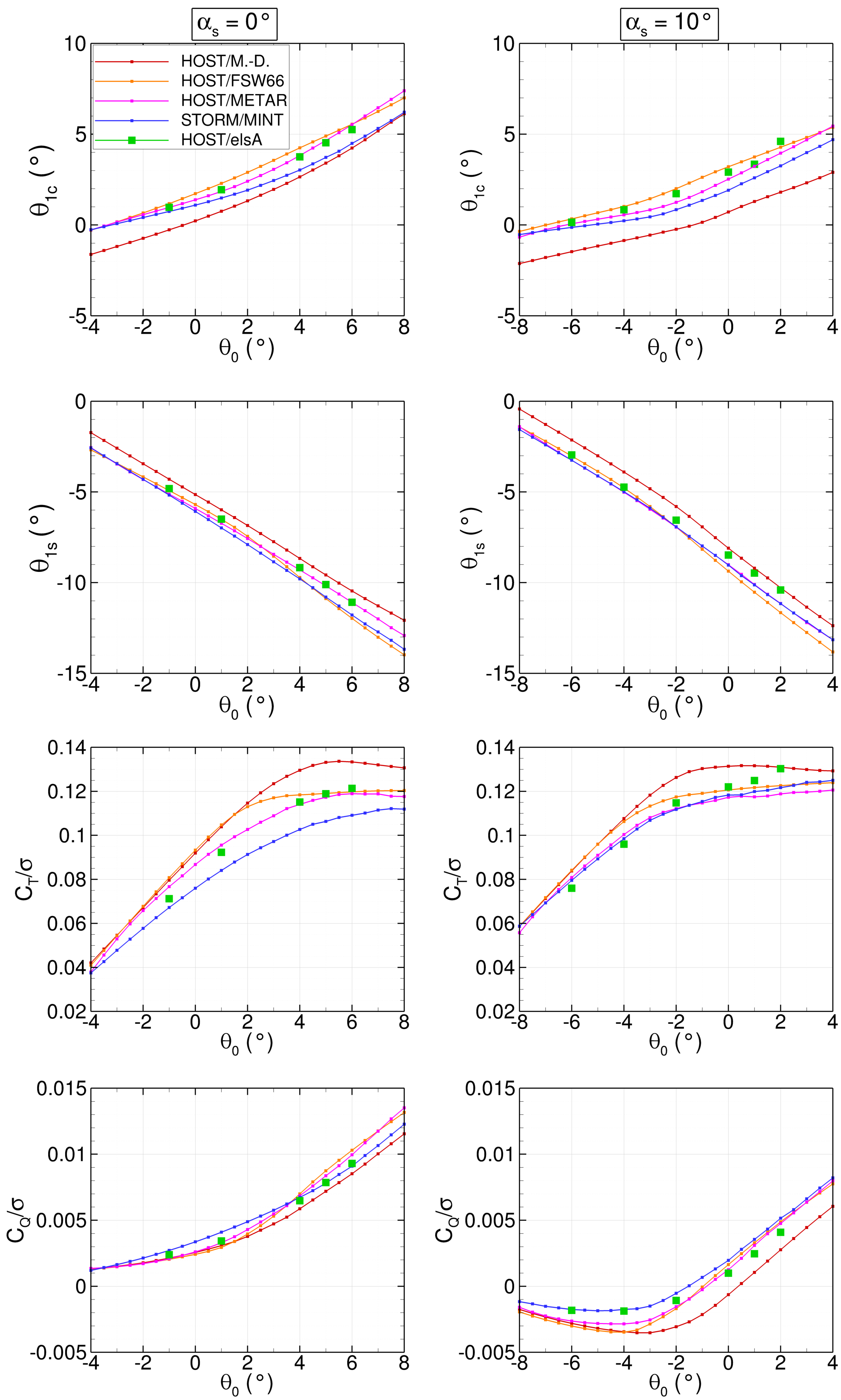

Figure 2: Polars of lateral cyclic pitch angle (first line), longitudinal cyclic pitch angle (second line), rotor thrust (third line) and power coefficients (fourth line) with respect to θ_0 for $\alpha_s = 0°$ (left) and $\alpha_s = 10°$ (right).

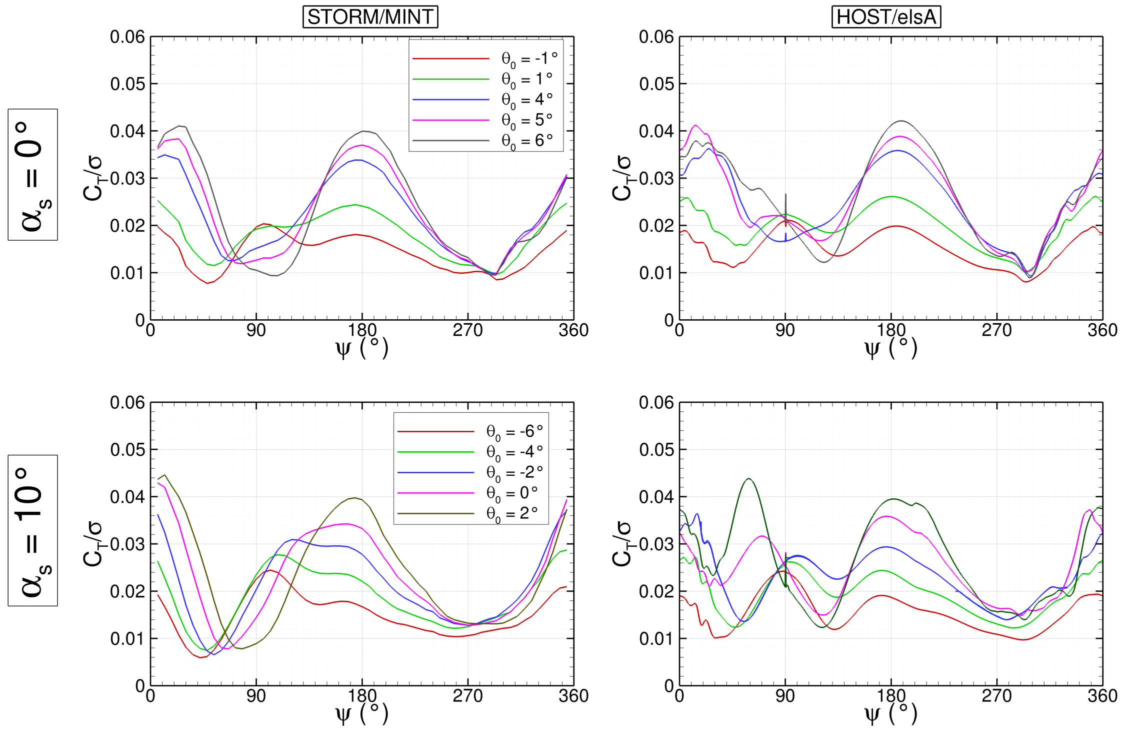

Figure 3: Blade thrust evolution obtained with STORM/MINT (left) and HOST/elsA (right) with respect to the blade azimuth for $\alpha_s = 0°$ (top) and $\alpha_s = 10°$ (bottom).

null to negative lift generation between $\psi = 30°$ and $\psi = 60°$. These two evolutions are also observed with STORM/MINT, with stronger amplitudes of lift variation with respect to the high-fidelity approach. This is confirmed by analysing the azimuthal evolution of C_nM^2 for this moderately-loaded case at different radial positions (cf. Fig. 6a). A good agreement is overall obtained between STORM/MINT and HOST/elsA for both the flat and tilted-backward rotor cases at all radial positions. The trends are confirmed to be similar, with the only differences observed being in terms of amplitudes obtained at specific locations. This plot also confirms that increasing the shaft angle for these moderately-loaded cases does not impact significantly the lift generation over the rotor disk.

At a second step, the results obtained at stronger load levels can be analysed using Fig. 5. First focusing on the flat rotor, Fig. 5 shows that similar rotor maps are obtained using the low- and high-fidelity approaches. Two main areas of positive lift generation situated on the rear blade (comprised between $\psi = -30°$ and $\psi = 30°$) and on the front blade (between $\psi = 180°$ and $\psi = 210°$) are visible. The azimuthal evolution of C_nM^2 plotted in Fig. 6b confirms that the trends are similar and that the main differences between STORM/MINT and HOST/elsA lie in the amplitude predicted. They also highlight a less visible difference situated close to the rear blade tip in the fourth quadrant, where a dynamic stall event predicted by the high-fidelity approach that leads to a significant decrease in lift generation close to $\psi = 330°$ is not visible with the low-fidelity approach. This dynamic stall event will be further investigated in the following paragraphs using pitching moment rotor maps. Focusing now on the backward-tilted rotor ($\alpha_s = 10°$), the agreement between STORM/MINT and HOST/elsA appears less satisfactory. Both approaches predict a region of positive lift generation on the rear blade close to $\psi = 0°$ with different extensions and amplitudes. Differences mainly appear on the results obtained on the front blade, with STORM/MINT predicting a region of high lift generation close to $\psi = 150°$ while HOST/elsA locates it close to $\psi = 180°$. In addition, close to $\psi = 60°$, the low-fidelity approach predicts small to negative values of lift generation while HOST/elsA predicts a third concentrated spot of high lift generation, which constitutes the main difference between the two approaches and will be further investigated in the next paragraph. The extension of the negative lift generation region on the rotor disk close to $\psi = 120°$ is also different between the two approaches. Fig. 6b also highlights that dynamic stall events occur in the fourth quadrant. Previous studies (Refs. 5, 15, 17) show that these events observed for both the flat and tilted-backward rotor are probably triggered by BVI. This will be further investigated in the next section using flow visualizations.

To better understand the differences observed between the low- and high-fidelity results, as well as investigate the local lift variation with an increase of the shaft angle, the evolution of the torsion deformation can be analysed. The rotor maps of this quantity for the different flight conditions simulated are plotted in Figs. 7 and 8 for the moderately- and highly-loaded cases respectively.

The observations on the moderately-loaded cases plotted in

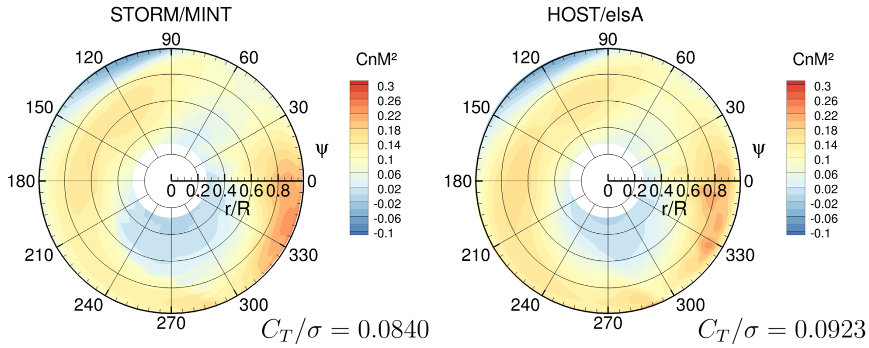

(a) $\theta_0 = 1°$, $\alpha_s = 0°$.

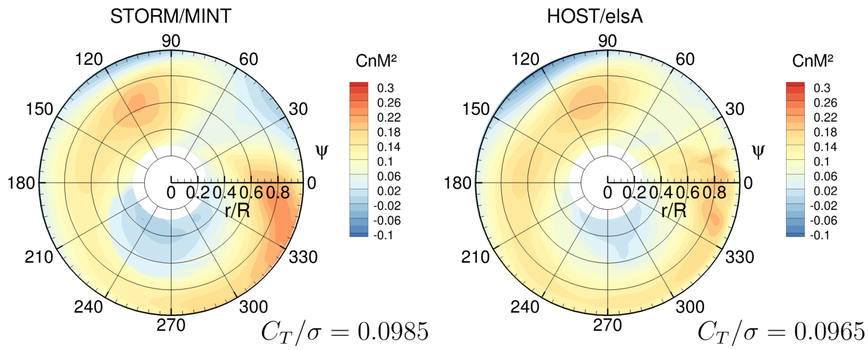

(b) $\theta_0 = -4°$, $\alpha_s = 10°$.

Figure 4: C_nM^2 rotor maps with respect to the blade azimuth for moderately- and highly-loaded cases.

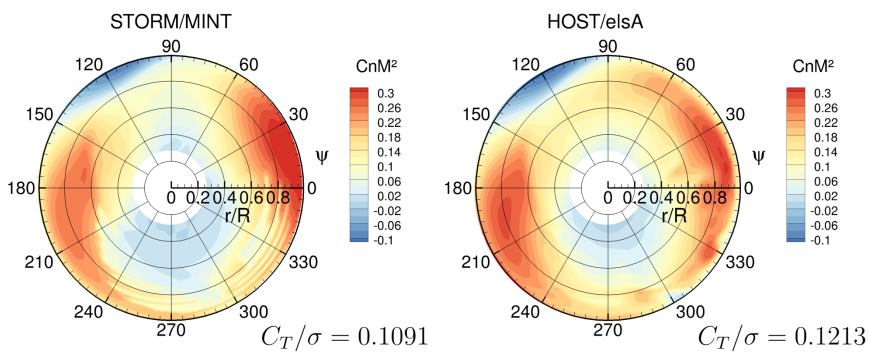

(a) $\theta_0 = 6°$, $\alpha_s = 0°$.

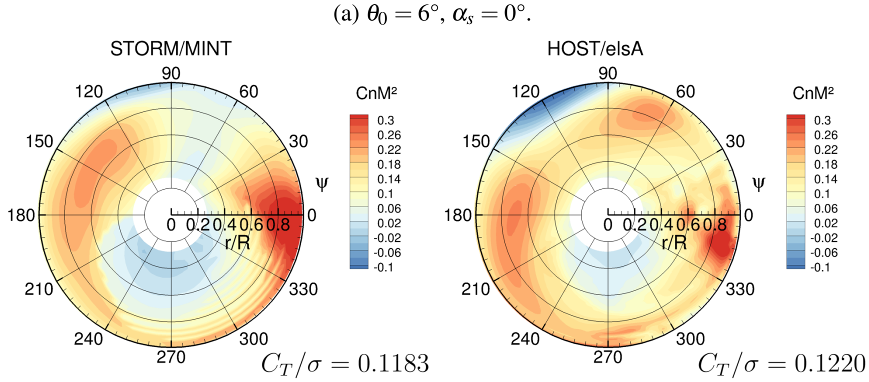

(b) $\theta_0 = 0°$, $\alpha_s = 10°$.

Figure 5: C_nM^2 rotor maps with respect to the blade azimuth for moderately- and highly-loaded cases.

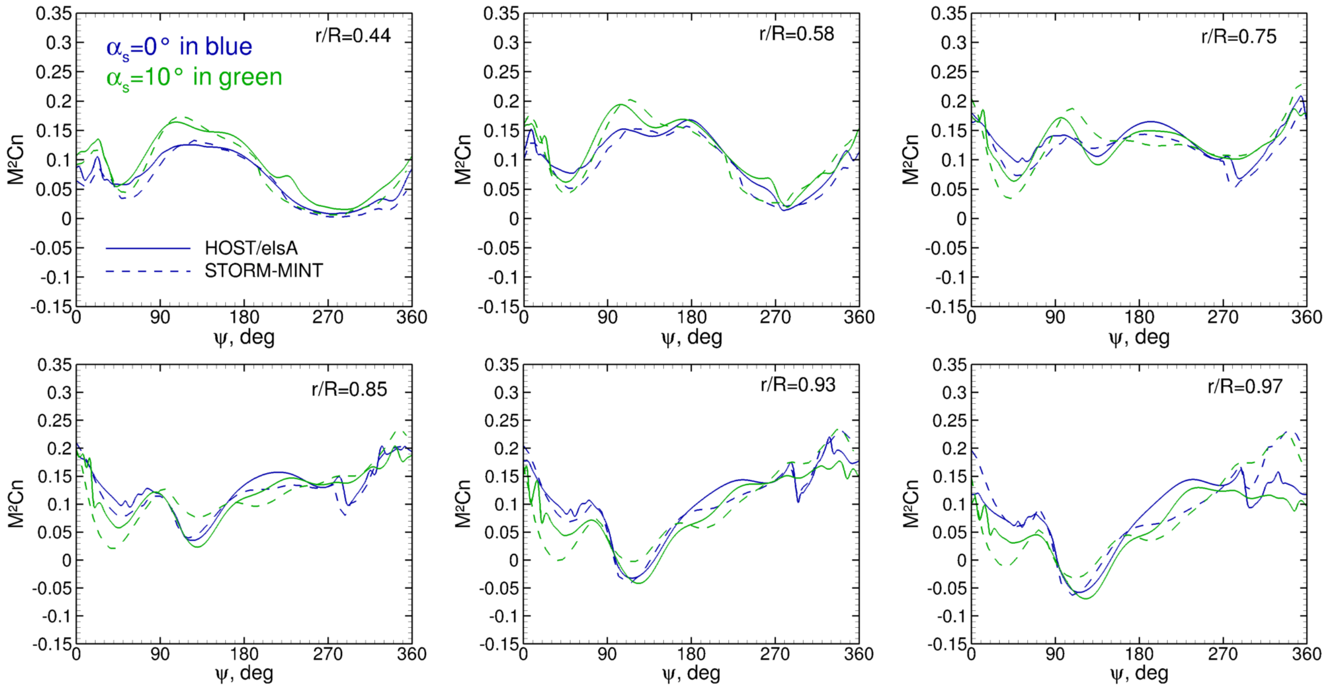

(a) Moderately-loaded cases ($(\alpha_s, \theta_0) = (0°, 1°)$ and $(\alpha_s, \theta_0) = (10°, -4°)$).

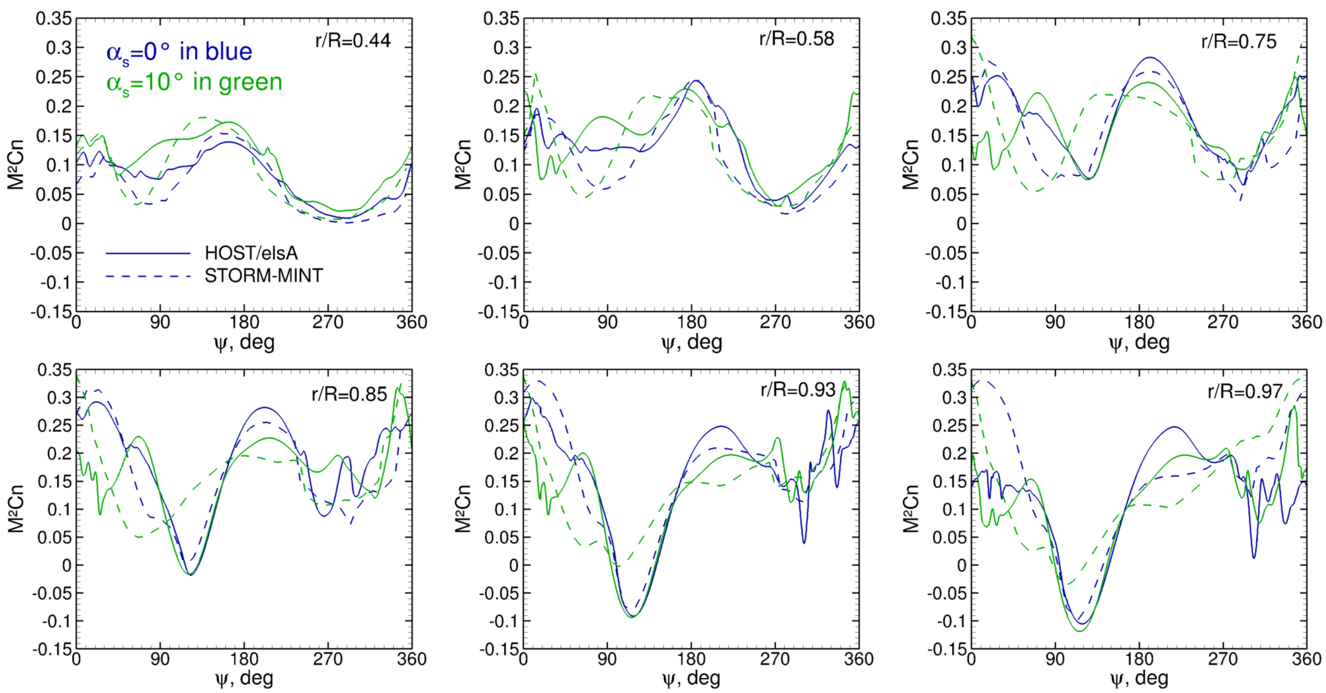

(b) Highly-loaded cases ($(\alpha_s, \theta_0) = (0°, 6°)$ and $(\alpha_s, \theta_0) = (10°, 0°)$).

Figure 6: $C_n M^2$ evolutions with respect to the azimuth for moderately- and highly-loaded cases.

Fig. 7 are similar to those discussed previously. The results obtained with the low- and high-fidelity approaches at both shaft angle values are similar, the main difference visible being the higher amplitude of the deformation predicted by HOST/elsA with respect to STORM/MINT. No significant effect due to the increase of the shaft angle is clearly visible either, as the rotor maps remain very similar between $\alpha_s = 0°$ and $\alpha_s = 10°$.

The results obtained for the highly-loaded cases on the other hand highlight several noticeable effects. Firstly, focusing on the results obtained for the flat rotor, the rotor maps remain very similar between the low- and high-fidelity approaches, with again higher amplitudes of deformation predicted by HOST/elsA. In addition, a small phase shift is visible in the fourth quadrant, with negative torsion predicted close to $\psi = 345°$ by STORM/MINT while HOST/elsA locates it close to 330°. Secondly, the results obtained for $\alpha_s = 10°$ highlight significant differences. Besides the fact that HOST/elsA predicts higher amplitudes of the deformation than STORM/MINT, and that a small phase shift of roughly 15° occurs for regions of similar torsion behavior, a significant difference in the results is visible at $\psi = 60°$. Indeed, a lobe of strong positive torsion deformation is visible with the high-fidelity approach, which is not captured in the low-fidelity results. Note that three direct effects from increasing the shaft angle are thus directly visible: the torsion deformation amplitude is increased, a phase shift of the deformation is visible for the positive torsion region situated in the first quadrant, and an additional lobe of positive torsion deformation appears at $\psi = 60°$.

The analysis of the torsion deformation is directly linked to the observations made on the $C_n M^2$ rotor maps showed in Figs. 4 and 5. Indeed, stronger positive and negative torsion deformations respectively lead to higher and lower angle of attack values, thus leading to higher (in the absence of flow separation) and lower local lift generation. The lobe of positive lift generation observed for $(\alpha_s, \theta_0) = (10°, 0°)$ with HOST/elsA at $\psi = 60°$ is for example directly due to the strong torsion deformation in this rotor disk region. Since this torsion excitation is not perceived in STORM/MINT, this directly leads to discrepancies in the prediction of local lift generation, and thus in rotor thrust coefficient near stall (cf. Fig. 3).

To investigate the origin of the richer torsion excitation predicted by CFD, the pitching moment coefficient $C_m M^2$ is plotted in the form of rotor maps and integrated values in Figs. 9 and 10. Since the excitation in torsion deformation is very low at moderately-loaded flight conditions, the $C_m M^2$ rotor maps corresponding to these cases are not shown (but the pitching moment evolution with respect to ψ is plotted).

For the highly-loaded flat rotor configuration, the retreating blade tip is characterised by strong negative pitching moment peaks extending from the middle to the tip of the blade. Both low- and high-fidelity approaches predict this trend between $\psi = 210°$ and $\psi = 360°$ (referred to as dynamic stall event DS1), with higher amplitudes visible with CFD. Strong variations of the section pitching moment also appear on high-fidelity results between $\psi = 0°$ and $\psi = 45°$ (referred to as DS2). Fig. 9 shows that this DS2 flow region does not appear on the low-fidelity results, an observation that will be discussed more extensively while analysing the phenomena responsible for this stall event using flow visualisations in the next section.

For $\alpha_s = 10°$, the dynamic stall event DS1 is also clearly visible on the retreating blade part of the rotor disk, which is again predicted at lower amplitudes by STORM/MINT with respect to HOST/elsA. The second dynamic stall event visible for the flat rotor is on the other hand not visible on the rotor maps. Instead, HOST/elsA predicts a second dynamic stall event DS2' close to $\psi = 0°$ which starts mid-span of the blade, with pitching moment fluctuations clearly visible towards the tip of the blade. Again, this trend is not reproduced by the low-fidelity approach, which appears to miss this effect that might be due to BVI.

To conclude on this part, STORM/MINT appears to be in very good agreement with HOST/elsA regardless of the shaft angle value for moderately-loaded cases. However for flight conditions which are close to dynamic stall, differences are visible between the two approaches. It appears that for both shaft angles investigated, STORM/MINT underestimates the torsion deformation resulting from dynamic stall events, thus leading to differences in terms of thrust value coefficients and of collective pitch angle values at which dynamic stall occurs. Differences in amplitude aside, a good agreement in terms of trends can still be observed in the rotor maps investigated for the flat rotor case, with the exception of a dynamic stall event DS2 that is not predicted by the low-fidelity approach. As this event is located is located close to the tip of the blade in the first quadrant, it does not impact significantly the aerodynamic performance and structural coefficients.

For the backward-tilted rotor investigation on the other hand, the agreement between both approaches is less satisfactory. The dynamic stall event DS2' is again not perceived by STORM/MINT, but is this time extended in the inner part of the rear blade. This leads to a different structural response observed over the rotor disk, and thus to the absence of a lobe of high thrust generation perceived by CFD at $\psi = 60°$. The weak CA/CFD coupling thus appears more adapted to accurately investigate the physics dominating dynamic stall.

DETAILED ANALYSIS OF THE MECHANISMS LEADING TO DYNAMIC STALL USING HIGH-FIDELITY RESULTS

The dynamic stall events leading to negative local $C_m M^2$ values are analysed in this section using rotor maps of separation length and location. For this purpose, the chordwise positions of flow separation in the upper side and the chordwise extent of the separation are shown for different values of θ_0 and α_s in Figs. 11 and 12.

At $\alpha_s = 0°$, these contours show that the dynamic stall event DS1 ($210° < \psi < 360°$) is related to a massive flow separation

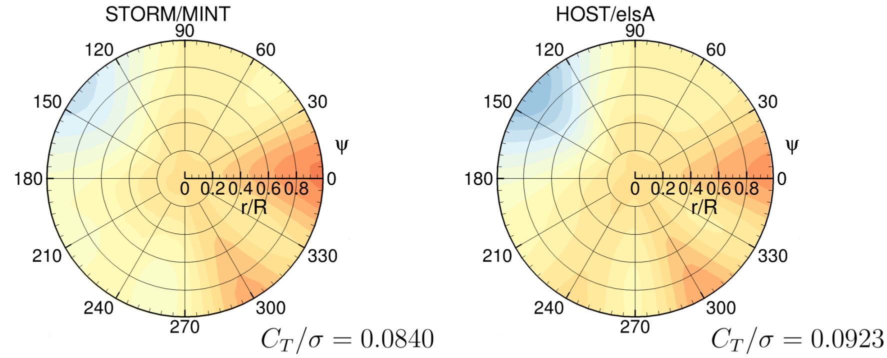

(a) $\theta_0 = 1°$, $\alpha_s = 0°$.

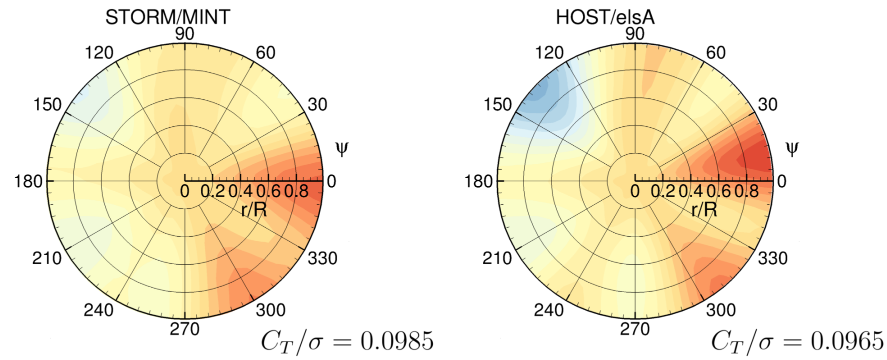

(b) $\theta_0 = -4°$, $\alpha_s = 10°$.

Figure 7: Rotor maps of torsion deformation for moderately- and highly-loaded cases.

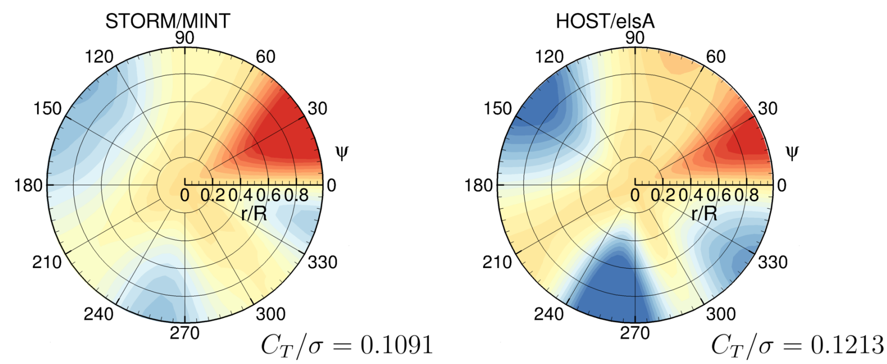

(a) $\theta_0 = 6°$, $\alpha_s = 0°$.

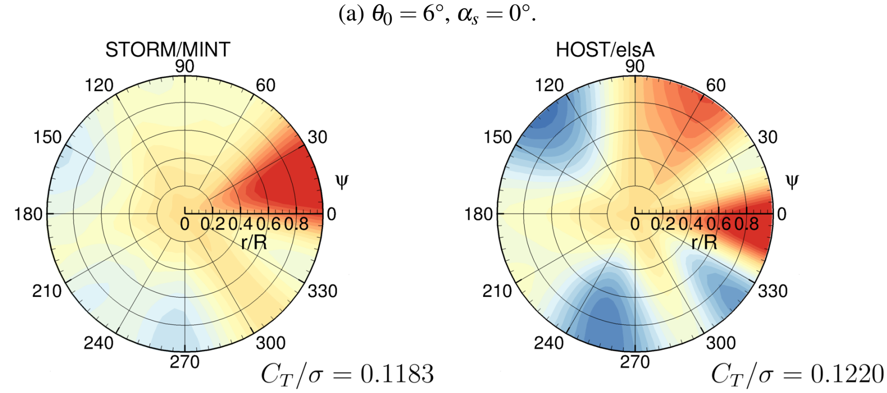

(b) $\theta_0 = 0°$, $\alpha_s = 10°$.

Figure 8: Rotor maps of torsion deformation for moderately- and highly-loaded cases.

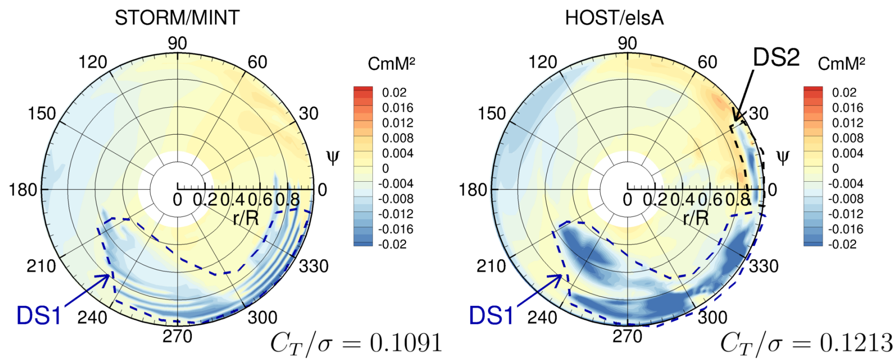

(a) $\theta_0 = 6°$, $\alpha_s = 0°$.

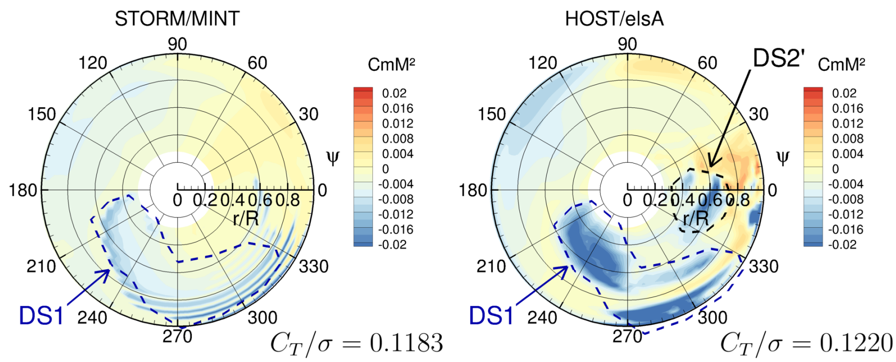

(b) $\theta_0 = 0°$, $\alpha_s = 10°$.

Figure 9: Rotor maps of pitching moment for moderately- and highly-loaded cases.

area that extends from the leading edge to the trailing edge as θ_0 increases. The second flow separation region, related to DS2 ($0° < \psi < 45°$), remains confined to the first half of the aerodynamic profiles of the blade (i.e. the flow reattaches upstream of the trailing edge). The associated flow separation initially appears isolated close to $\psi = 30°$, and its extension with the increase of collective pitch angle leads to a merge of this flow separation region with the one associated to DS1. Increasing the shaft angle to $\alpha_s = 10°$ shows that the development of the dynamic stall event DS1 as θ_0 increases is very similar to the one observed at $\alpha_s = 0°$. They are thus likely to be associated to a similar physical phenomenon. The fluctuations associated to the dynamic stall event DS2' ($\psi \approx 0°$) appear as distributed along the blade span, and the phenomenon is extended on the rotor disk area as θ_0 increases with flow separated along the complete airfoil sections.

The dynamic stall mechanisms responsible for these observations can be investigated in detail using flow visualisations. For this purpose, Figs. 13 and 14 show Q-criterion isosurfaces and vertical velocity fields one chord below the rotor obtained with HOST/elsA at several collective pitch angles values for the flat and tilted rotor positions. They highlight that the flow separation in the area DS1 is triggered by a BVI, which starts at the inner blade sections ($\psi = 210°$) and spreads along the whole blade as the BVI region moves towards the blade tip. This is observed for both the flat and backward-tilted rotor positions, and is also observed in the literature (Ref. 9). At $\alpha_s = 0°$, the second flow separation area DS2 also appears to be due to a BVI with a vortex emanating from the root of the three preceding blades, which seem to merge with dynamic stall vortices coming from the fourth preceding blade as they convect towards the affected blade tip. This effect combined with the high torsion deformation values observed above thus leads to the flow separation observed in Fig. 11. As for the case $\alpha_s = 10°$, Fig. 14 shows that the DS2' dynamic stall event does not appear as part of the blade root vortices incriminated are convected above the rotor blade due to the inclination. Yet, the dynamic stall vortices generated close to $\psi = 270°$ as well as the root vortex of the preceding blade are again convected towards the front blade in the first quadrant, leading to BVI in the inner part of the blade. Thus, the origin of this dynamic stall event remains similar, even though the patterns leading to it are different. A last BVI interaction occurs close to $\psi = 90°$ due to the tip vortex of the preceding blade, which leads to a small flow separation towards the tip of the blade (also appearing in Fig. 12). It should also be noted that the vortex structures and velocity field appear significantly more chaotic in the backward-tilted rotor case with respect to the flat one when dynamic stall occurs.

Consequently, the dynamic stall events DS2 and DS2' are both due to BVI, and are specifically provoked by root vortices and dynamic stall vortices interacting with the rotor blade. Considering the rotor hub inside the simulation could lead to the disappearance of the root vortices, or at least re-

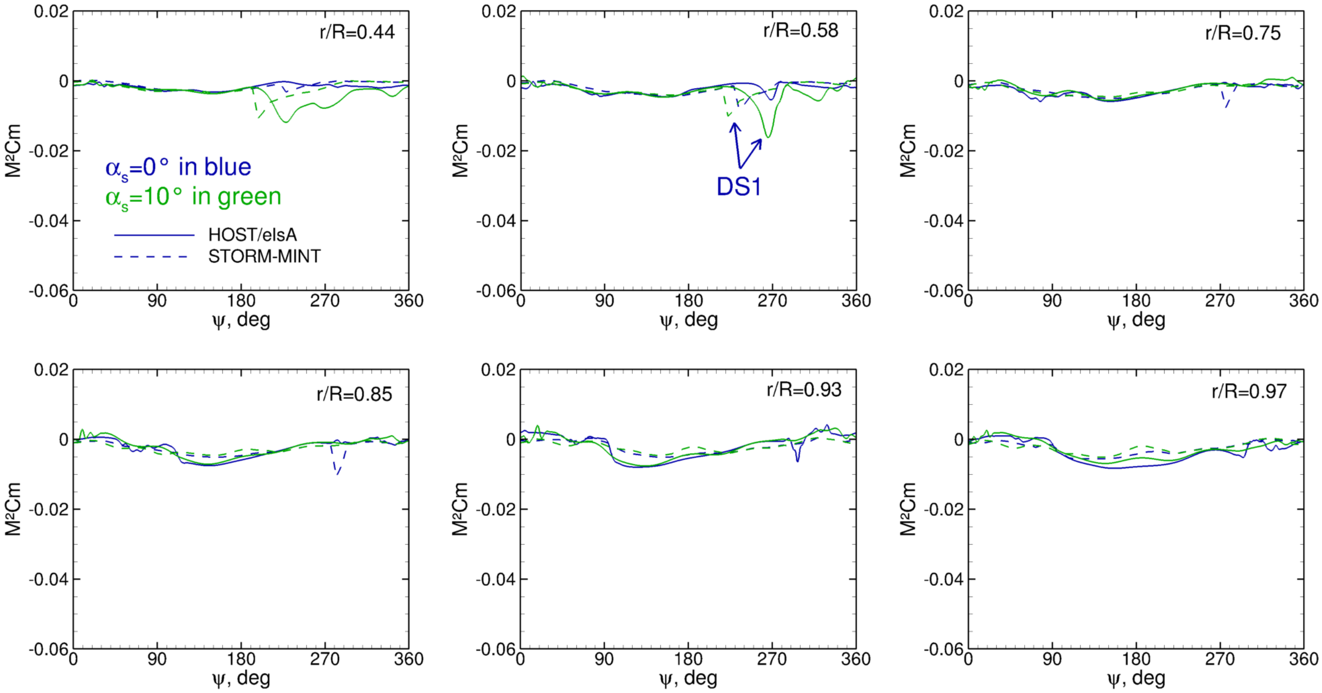

(a) Moderately-loaded cases ($(\alpha_s, \theta_0) = (0°, 1°)$ and $(\alpha_s, \theta_0) = (10°, -4°)$).

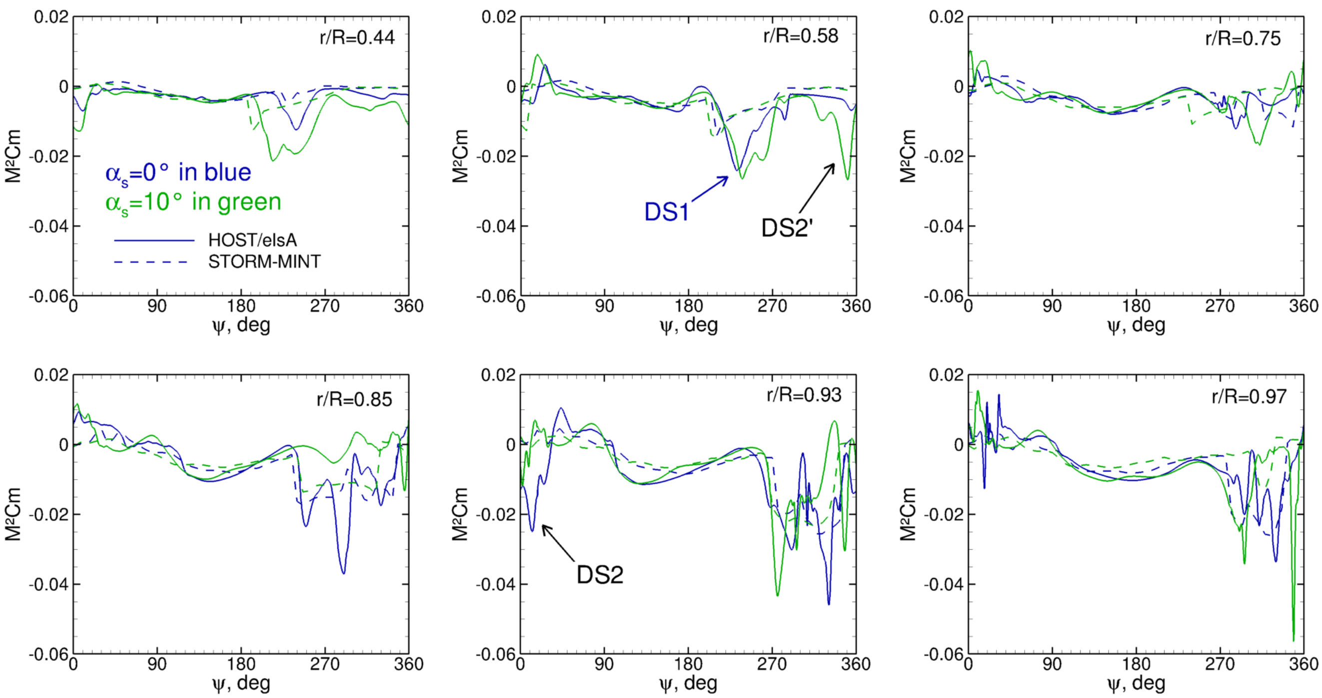

(b) Highly-loaded cases ($(\alpha_s, \theta_0) = (0°, 6°)$ and $(\alpha_s, \theta_0) = (10°, 0°)$).

Figure 10: $C_m M^2$ evolutions with respect to the azimuth for moderately- and highly-loaded cases.

duce their strength and their effect on the rear blade where the second dynamic stall event occurs.

CONCLUSIONS

This paper presented an analysis of the impact of a positive rotor shaft angle on dynamic stall for a generic helicopter rotor test case using low- (STORM/MINT) and high-fidelity (HOST/elsA) approaches. Two objectives were pursued: to evaluate the capability of the low-fidelity approach to investigate dynamic stall under these flight conditions using the high-fidelity results as reference, and to identify the physical mechanisms responsible for dynamic stall using HOST/elsA. Several conclusions are drawn from this study:

1. Dynamic stall is primarily driven by BVI for both the flat and backward-tilted positions of the rotor. A commonly-observed dynamic stall event due to BVI occurs in the third quadrant for both shaft angles. A second dynamic stall event occurs in both cases due to the interaction between dynamic stall and root blade vortices. Tilting the rotor backward however leads to a different type of BVI on the rear blade, which is then located in the inner part of the blade instead of close to the blade tip.

2. The dynamic stall event occurring in the third quadrant is predicted by STORM/MINT, albeit with a lower intensity. More generally, for regions excluding the second dynamic stall event, the agreement between STORM/MINT and HOST/elsA is satisfactory, with similar trends obtained. The main difference in these regions is an underestimation of the different structural and aerodynamic coefficients with respect to HOST/elsA.

3. The second dynamic stall event on the other hand is not correctly represented by STORM/MINT for both shaft angles. The pitching moment is consequently different in that region compared to the results obtained with HOST/elsA. This has direct consequences on the torsion deformation dynamics and thus on the local lift generation across the rotor disk.

4. For $\alpha_s = 0°$, the STORM/MINT rotor maps show similar trends of lift generation with respect to HOST/elsA. This is because the second dynamic stall event is concentrated at the blade tip in a small region of the first quadrant, thus leading to small differences in the torsion and normal section force contours.

5. For $\alpha_s = 10°$, the agreement between STORM/MINT and HOST/elsA rotor maps of lift generation is less satisfactory. This is because the second dynamic stall event is this time more extended as it occurs in the inner part of the blade in the first quadrant. This leads to non-negligible differences in terms of torsion deformation (and thus section normal force) in the first quadrant of the rotor map.

6. In terms of polar, the results are similar at both shaft angles. The agreement is satisfactory between the low- and high-fidelity approaches at low values of collective pitch angles. The linear region slopes and the collective pitch angle above which dynamic stall start occurring are however found to be different. Consequently, different rotor thrust values reached after dynamic stall are predicted by the two approaches. This discrepancy is explained by the different observations proposed above.

In addition to the shaft angle effect, the helicopter velocity impact on dynamic stall is investigated in (Ref. 16). Several works could be performed in the future to complete these two studies. Firstly, the effect from tilting the rotor forward (negative shaft angle, i.e. propulsive rotor) on the physical phenomena leading to dynamic stall could be investigated. This would also allow to investigate the capacity of STORM/MINT to give representative results on such a flight configuration. Other helicopter translation velocities could also be simulated to complete this study. This would allow to investigate potential trends on the dynamic stall occurrence with increasing speed. Finally, additional components of the helicopter (such as rotor hub, fuselage, etc) could be considered in the simulations to investigate the effect obtained on dynamic stall.

Author contact:
Ilyès Berhouni ilyes.berhouni@onera.fr
Joëlle Bailly joelle.zibi@onera.fr
François Richez francois.richez@onera.fr

ACKNOWLEDGMENTS

The authors would like to acknowledge the European Union that has funded this research activity in the frame of the ENGRT (European Next Generation Rotorcraft Technology) project and Manousos Kelaidis from Airbus Helicopters for his sound advice during this study.

REFERENCES

1. M. Balmaseda, H. Yeo, F. Richez, B. Jayaraman, and B. Ortun. High-fidelity aerodynamic loads analysis of the double-swept ERATO rotor. In *50th European Rotorcraft Forum*, Marseille, France, 2024. URL: https://hal.science/hal-04783292.

2. P.-M. Basset, O. Heuze, J.V.R. Prasad, and M. Hamers. Finite State Rotor Induced Flow Model for Interferences and Ground Effect. In *Proceedings of the American Helicopter Society 57th Annual Forum*, Washington DC, United States, 2001.

3. B. Benoit, A.-M. Dequin, K. Kampa, W. von Grünhagen, P.-M. Basset, and B. Gimonet. HOST, a General Helicopter Simulation Tool for Germany and France. In *56th American Helicopter Society Annual Forum*, Virginia Beach, United States, 2000.

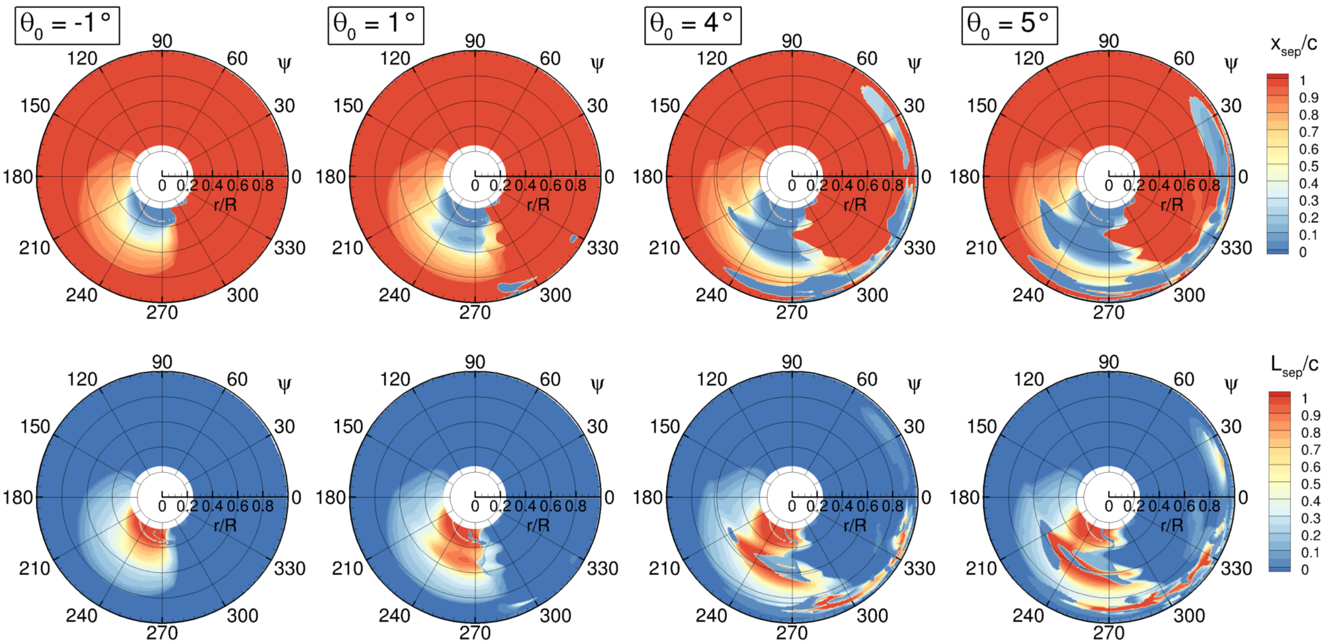

Figure 11: Rotor maps of separation point location and length for different values of θ_0 for $\alpha_s = 0°$.

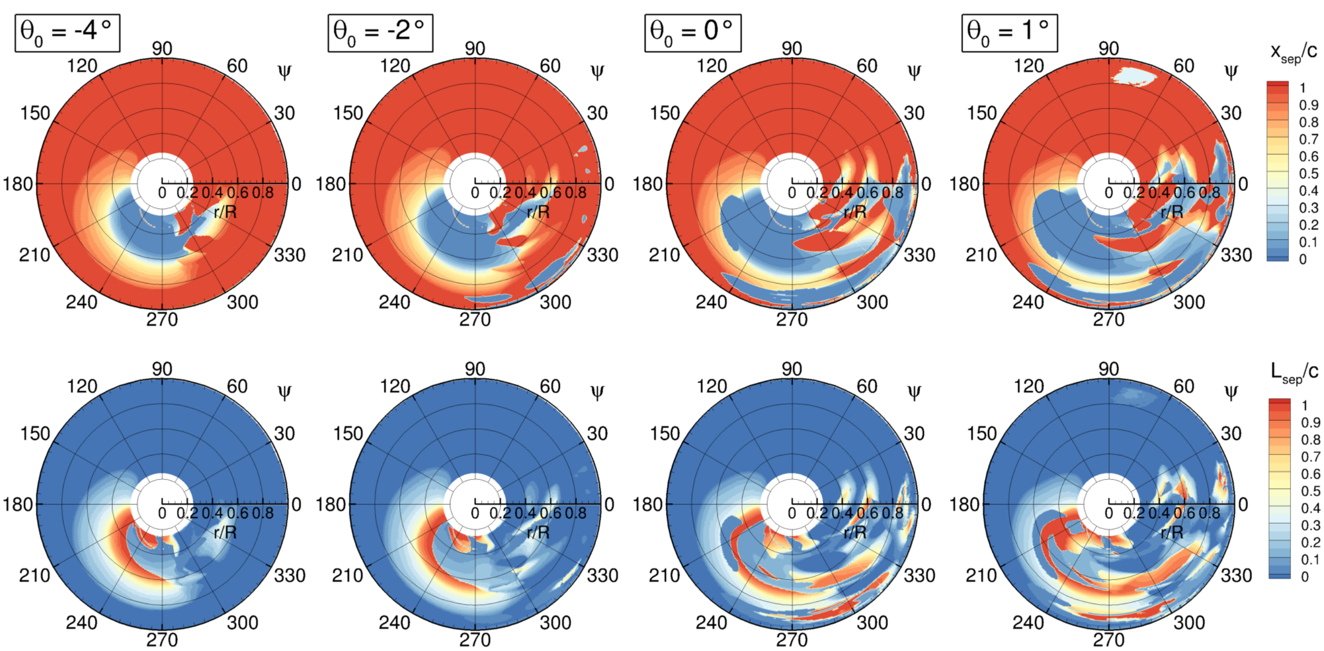

Figure 12: Rotor maps of separation point location and length for different values of θ_0 for $\alpha_s = 10°$.

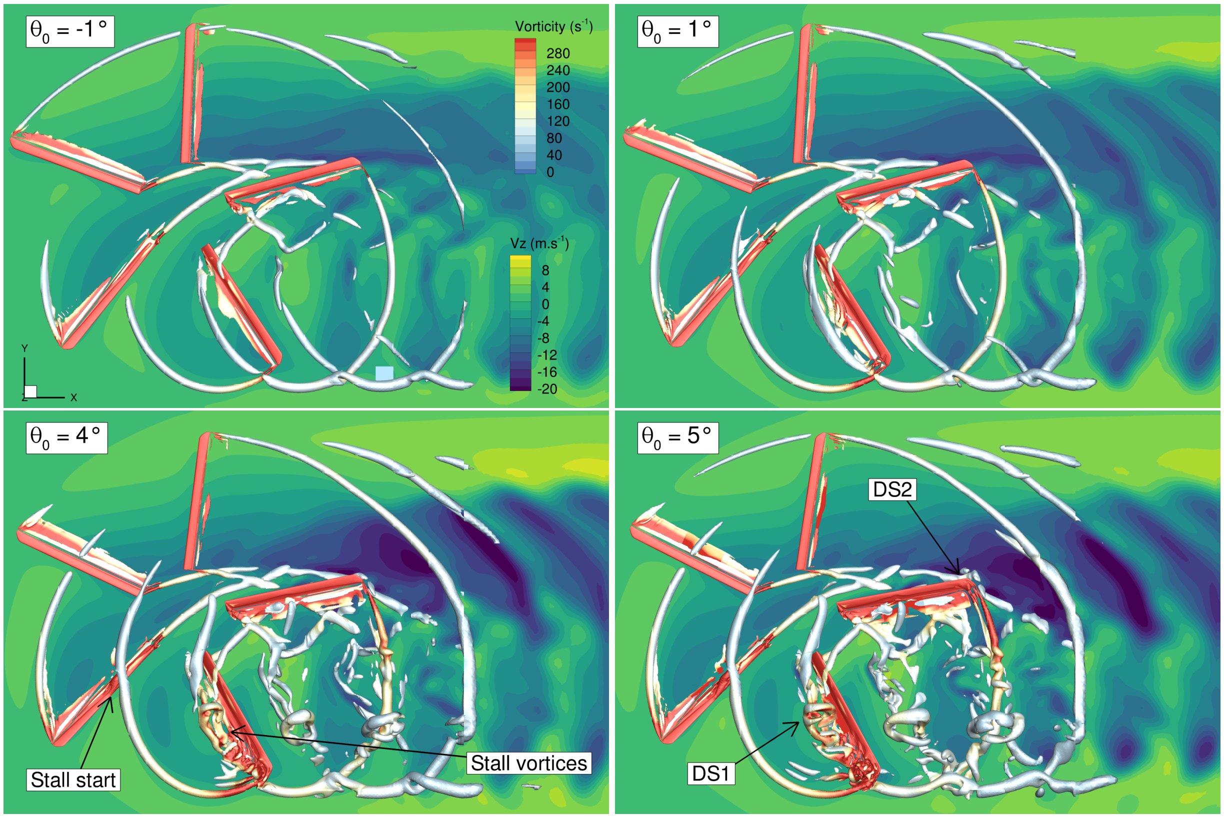

Figure 13: Q-criterion colored by vorticity magnitude and vertical velocity contour one chord below the rotor for $\alpha_s = 0°$.

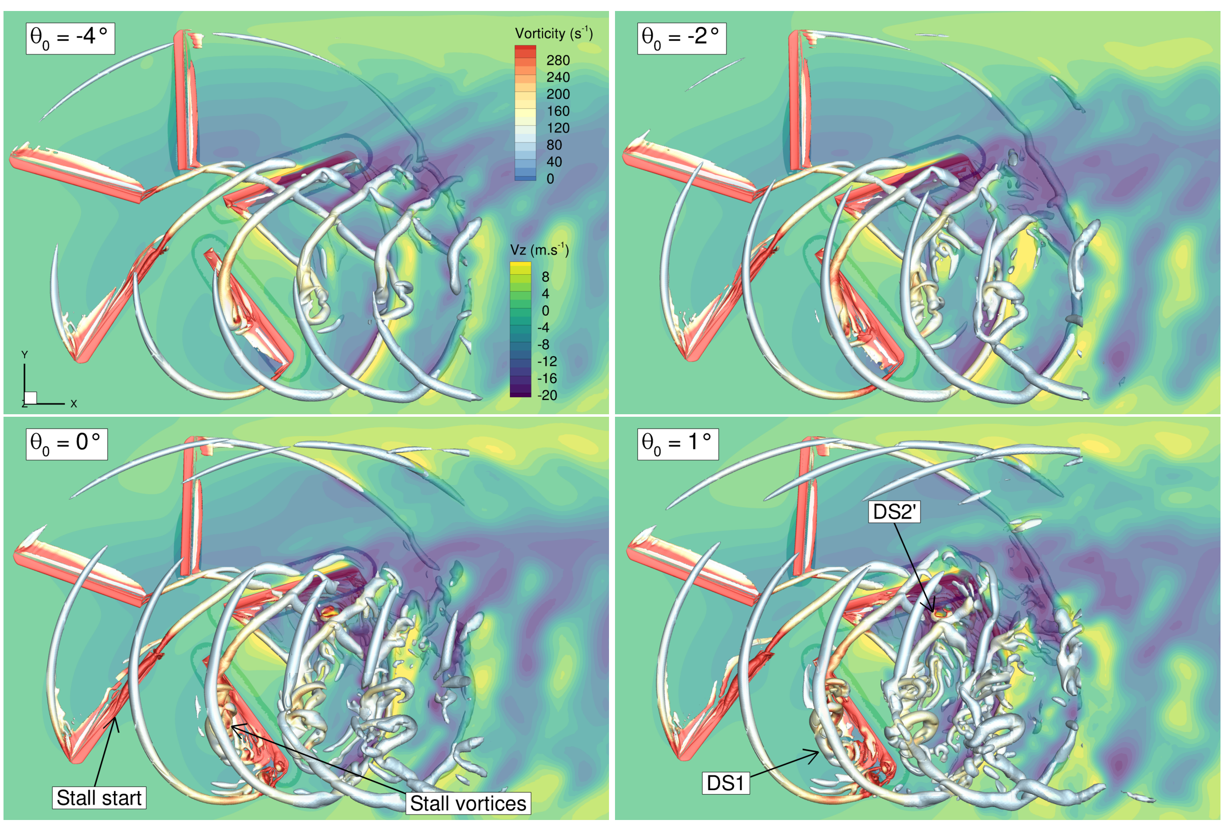

Figure 14: Q-criterion colored by vorticity magnitude and vertical velocity contour one chord below the rotor for $\alpha_s = 10°$.

4. L. Cambier, S. Heib, and S. Plot. The Onera elsA CFD software: input from research and feedback from industry. *Mechanics & Industry*, 14(3):159–174, 2013. doi:10.1051/meca/2013056.

5. C. Castells, F. Richez, and M. Costes. A Numerical Analysis of the Dynamic Stall Mechanisms on a Helicopter Rotor from Light to Deep Stall. *Journal of the American Helicopter Society*, 65(3):1–17, 2020. doi:10.4050/jahs.65.032005.

6. P. Eglin, M. Embacher, D. Desvigne, and E. Roca-Leon. Airbus RACER High Speed Demonstrator Flight Tests. In *Proceedings of the Vertical Flight Society 81st Annual Forum and Technology Display*, Virginia Beach, United States, 2025. doi:10.4050/f-0081-2025-182.

7. J. C. Kok. Resolving the Dependence on Freestream Values for the k-ω Turbulence Model. *AIAA Journal*, 38(7):1292–1295, 2000. doi:10.2514/2.1101.

8. G. Le Bouar, M. Costes, A. Leroy-Chesneau, and P. Devinant. Numerical simulations of unsteady aerodynamics of helicopter rotor in manoeuvring flight conditions. *Aerospace Science and Technology*, 8(1):11–25, 2004. doi:10.1016/j.ast.2003.08.004.

9. J. Letzgus, M. Keßler, and E. Krämer. Simulation of Dynamic Stall on an Elastic Rotor in High-Speed Turn Flight. *Journal of the American Helicopter Society*, 65(2):1–12, 2020. doi:10.4050/jahs.65.022002.

10. P. Lorber, C. Matalanis, G. Law, J. O'Neill, and P. Bowles. Overview of S-97 RAIDER Scale Model Tests. In *Proceedings of the Vertical Flight Society 72nd Annual Forum*, West Palm Beach, United States, 2016. doi:10.4050/f-0072-2016-11559.

11. F. R. Menter. Two-equation eddy-viscosity turbulence models for engineering applications. *AIAA Journal*, 32(8):1598–1605, 1994. doi:10.2514/3.12149.

12. B. Ortun, M. Potsdam, H. Yeo, and K. V. Truong. Rotor Loads Prediction on the ONERA 7A Rotor Using Loose Fluid/Structure Coupling. *Journal of the American Helicopter Society*, 62(3):1–13, 2017. doi:10.4050/jahs.62.032005.

13. M. Potsdam, A. Datta, and B. Jayaraman. Computational Investigation and Fundamental Understanding of a Slowed UH-60A Rotor at High Advance Ratios. *Journal of the American Helicopter Society*, 61(2):1–17, 2016. doi:10.4050/jahs.61.022002.

14. M. Potsdam, H. Yeo, and W. Johnson. Rotor Airloads Prediction Using Loose Aerodynamic/Structural Coupling. *Journal of Aircraft*, 43(3):732–742, 2006. doi:10.2514/1.14006.

15. F. Richez. Analysis of Dynamic Stall Mechanisms in Helicopter Rotor Environment. *Journal of the American Helicopter Society*, 63(2):1–11, 2018. doi:10.4050/jahs.63.022006.

16. F. Richez, J. Bailly, and I. Berhouni. Evaluation of speed effect on dynamic stall based on low and high fidelity aeroelastic rotor simulations. In *51st European Rotorcraft Forum*, Venise, Italy, 2025.

17. F. Richez, R. Jain, M. Smith, A. Grubb, and C. Castells. Validation and Analysis of Aeroelastic Simulations of the UH-60A Rotor from Pre-to Post-stall Flight Conditions. In *76th Annual Forum & Technology Display (Vertical Flight Society)*, Virginia Beach, United States, 2020. URL: https://hal.science/hal-03103937.

18. H. Yeo, M. Balmaseda, B. Jayaraman, F. Richez, and B. Ortun. High-fidelity structural loads analysis of the double-swept ERATO rotor. In *50th European Rotorcraft Forum*, Marseille, France, 2024. URL: https://hal.science/hal-04783322.

19. H. Yeo, M. Potsdam, B. Ortun, and K. V. Truong. High-Fidelity Structural Loads Analysis of the ONERA 7A Rotor. *Journal of Aircraft*, 54(5):1825–1839, 2017. doi:10.2514/1.c034286.

CLASSIFICATION & COPYRIGHT